# Nanotextured aluminium based surfaces with icephobic properties

Michael GRIZEN[1], Tanmoy MAITRA[1], Jeremy P. BRADLEY[2], Manish K. TIWARI[1,3*]

*Corresponding author: Tel.: +44 (0)20131 081056; Email: m.tiwari@ucl.ac.uk

[1]Nanoengineered Systems Laboratory, UCL Mechanical Engineering, University College London, Torrington Place, London, WC1E 7JE, UK
[2]Airbus Operations Ltd, Pegasus House, Aerospace Avenue, Filton, Bristol, BS34 7PA, UK
[3]Wellcome/EPSRC Centre for Interventional and Surgical Sciences (WEISS), University College London, London, W1W 7TS, UK

Abstract Undesirable water freezing (icing) usually occurs in cold environments and may have lethal consequences. Preventing icing usually requires the installation of active thermal systems which consume energy and increase costs. Nanoengineered superhydrophobic surfaces can delay freezing passively; however, when exposed to sub-zero temperatures, they can get covered by frost, which promotes ice formation and impairs their icephobicity. Additionally, high thermal conductivity of the surfaces can reduce the frost formation rate. Thus, we chose aluminium as our working material for its good thermal conductivity and widespread industrial usage. We employed electrochemical anodization process to control and tune the surface morphology. Crucially, we demonstrate the feasibility of morphology control at the nanoscale and tunability of the surface solid fraction in the range of 0.1 – 0.25, while using safer polishing electrolytes and etchants compared to existing practice, i.e., our approach is environmentally friendlier. Surface functionalisation and morphology control were used to render the surfaces (super)hydrophobic, with low contact angle hysteresis. The best performing surfaces demonstrate ice nucleation temperatures as low as -19 °C and resist liquid impalement – tested via drop impact velocity up to 3 m/s (Weber number > 300) – demonstrating a clear potential for their exploitation as icephobic surfaces.

## Introduction

Ice formation, typical of sub-zero temperature environments, influences systems ranging from infrastructure to aviation. While being desirable in a number of applications, such as healthcare or food, it is unwelcome in others. For instance, the heat transfer performance of air conditioning and refrigeration systems can be severely reduced if the fins of the heat exchangers are covered with frost. The frost layer not only increases thermal resistance between the flowing air and the fins but can also obstruct the channel paths reducing the airflow [1, 2]. In addition, in the aviation industry,

ice accumulated on the aeroplane parts adds extra weight and significantly worsens the performance of aerodynamic bodies. Moreover, ice formation on flight controls of aircraft, hamper the aircraft's control, with fatal consequences. Therefore, to keep the vulnerable parts ice-free, aviation industry relies on active thermal control systems. The systems range from circulating bleed-air, i.e. the hot air from the engine, to electrothermal systems which pass electric current or deicing boots that inflate with compressed air to dislodge the ice accumulated on surfaces. What is common to all these systems is that they require complicated design and careful maintenance, and additional energy resulting in excessive fuel consumption [3]. Consequently, a passive anti-icing technique is of considerable interest. Therefore, designing icephobic surfaces is a potentially viable strategy. Depending on the application, an icephobic surface needs to have three different features: delay ice formation, offer low ice adhesion and resist freezing and impalement of supercooled water drops. Firstly, delaying ice nucleation giving more time for the droplets to roll-off [4]. Secondly, for surfaces with ice adhesion strength well below 100 kPa passive ice removal, for instance, by a mild wind becomes feasible [5, 6]. Lastly, an icephobic surface should resist impalement by water drops impacting at different velocities and temperatures because if the drops penetrate the surface texture, their freezing is inevitable [6]. Whereas achieving a subset of these features is highly useful, achieving all of them simultaneously is nontrivial and requires a rational, thermodynamically guided approach. The reason for such versatile requirements stems from different pathways through which the ice is formed and the nature of the 'ice' (supercooled liquid water and water vapour can change into different forms of ice depending on the conditions) [6, 7]. Even when the simplest environment is assumed, and any kind of contamination is ignored, when starting from water vapour there are two ice formation mechanisms. Water vapour can either condense and, if not removed, solidify (condensation and freezing) or solidify straight from the

vapour phase (desublimation) creating a frost layer.

There are several strategies to achieve icephobicity. Very recently, researchers proposed a strategy that utilized solar thermal energy to mitigate ice and frost layer from the surface [8, 9]. In this method, coatings were developed to absorb and confine solar energy into a small volume, leading to a rapid increase of the surface temperature. The rise in interfacial temperature effectively inhibits the frost formation, delays icing and sheds ice effectively. Although the technique shows promises as an effective icing mitigation strategy, its applicability in realistic conditions needs to be evaluated.

Most of the passive ice mitigation strategies, however, are based on the control of the surface design and wettability. As was summarized in [10], icephobic surfaces can be classified into three categories; smooth, textured or slippery. Each category has advantages and drawbacks depending on the environmental conditions. Therefore, the adopted strategy should be fit for a specific application. In this work, we are interested in aviation applications where the air flow, which can carry sand and dust particles, and the drop impacting velocity is very high. Hence, the paramount requirement of the icephobic surfaces in our case is to have high mechanical durability. The way the slippery surfaces are fabricated is initially, the substrate is textured, and then a water-immiscible and low surface energy lubricant is infused into the micro texture so that a thin liquid layer covers the surface. However, if such surfaces are constantly bombarded with particles or exposed to excessive shear force, the lubricant will be pushed outside, and the surfaces will lose the icephobic properties [10]. Smooth solid surfaces are another choice as they have good mechanical robustness. However, they display limited hydrophobicity – essentially dictated by

surface energy – which means that when supercooled droplets spread during the impact, they are more likely to freeze and stick to the surface [11].

Contrary to slippery and smooth surfaces which all have a flat air-substrate interface, textured surfaces can have different interfaces. The morphology of the textured surfaces can be tailor-made so that it can be nicely ordered or disordered and have micro or/and nanoscale features. When dealing with textured surfaces, extra care should be taken when characterizing them. The reason is that these surfaces are characterized by liquid wettability metrics such as water drop contact angle (CA) and contact angle hysteresis (CAH), and there are several drawbacks to such characterization. First of all, ice isn't necessarily formed through a liquid phase, making such characterization irrelevant. Additionally, what is even more problematic is that different morphologies may exhibit identical CA and CAH values and yet perform differently under different conditions. In fact, there are contradictory reports on ice adhesion and its relation to surface texture. Some authors claim that textured surfaces increase ice adhesion [12], whereas others claim the opposite [13, 14]. Through a systematic study, Subramanyam et al. [14] recently showed that the roughness scale plays a pivotal role in deciding the adhesion strength, and reported a better reduction in ice adhesion nanotextured superhydrophobic surfaces.

Furthermore, a number of studies have reported that surfaces with properly engineered micro- and nanoscale roughness can retard ice formation in the first place, which makes them superior to the smooth and slippery surface [15, 16]. Here again, a number of prior works [4, 17] have established the need for precise texture control in order to delay ice formation substantially and observed that smooth surfaces may farewell to this end. However, as was previously mentioned, the advantage

of the hydrophobic surfaces is clear when dealing with impacting droplets. More specifically, superhydrophobic surfaces, with contact angles greater than 150° and exhibiting roll-off angles less than 10° can delay ice formation by driving supercooled water drops away and thus reduce nucleation events [11, 16, 18]. As an additional layer of complexity, as aforementioned, when dealing with saturated environments, even without any precipitation, after a certain time frosting will appear on surfaces. Clearly, when the surfaces are covered with frost, their hydrophobicity and the ability to further delay freezing is lost. Therefore, preventing or at least delaying frost formation together with reducing ice adhesion are important features for an icephobic surface.

A particularly interesting phenomenon is associated with freezing of supercooled drops in low (unsaturated) humidity conditions. Under such conditions, the cold drops tend to evaporate, and evaporation is particularly strong when the freezing process commences because it releases heat. This was shown to result in a beautiful vapour halo during recalescent freezing of drops on thermally insulating substrates [19]. Low thermal conductivity made it harder for the latent heat of freezing to get transmitted through the substrate, and therefore, facilitated its absorption by the freezing droplet. Consequently, the evaporation rate was amplified. The resulting vapour from the drop was naturally formed in a cold environment and subsequently condensed down in a ring pattern around the mother droplet and froze. This resulted in the formation of a thin, ring-like frost layer around the mother drop. The frost ring, then, could initiate freezing of any neighbouring drops upon contacting them. The experiments also demonstrated that the frozen ring formation was intimately related to the thermal conductivity of the substrate on which the drop rested [19]. Specifically, smaller rings were formed around droplets freezing on surfaces with higher thermal conductivity; in fact, at high enough thermal conductivity no frozen rings were formed. The reason

for this is that latent heat released in the phase change process can be conducted through the substrate. Therefore, when considering anti-icing applications, a higher substrate conductivity is desirable and may help limit frost propagation through frozen ring formation around an individual freezing droplet out of an array.

In addition to the above-mentioned advantage, applications such as aerospace and infrastructure demand use of metallic substrates such as aluminium, which have excellent thermal conductivity. Therefore, the current work is focussed on manufacturing aluminium based icephobic surfaces. The approached is comprised of using safe chemicals to polish aluminium foils, followed by anodization [20] in oxalic or sulfuric acid baths. The anodized surfaces were immersed in a phosphoric acid solution to widen the pores and, thereby, control the surface solid fraction. Surface functionalisation using fluorosilanes was used to render the surfaces hydrophobic and/or superhydrophobic depending on the surface solid fractions. The resulting surfaces were characterized by wettability measurements comprising water drop advancing and receding contact angle, and contact angle hysteresis measurements, followed droplet impact tests to ascertain their stability in dynamic conditions. Finally, all surfaces were subjected to the freezing delay test in a custom designed, bench-top icing chamber.

# Experimental

## Materials

Aluminium sheets (0.5 mm thick and 99.99% purity) were purchased from Alfa-Aesar. Acetone, isopropyl alcohol, n-hexane, oxalic acid ($C_2H_2O_4$), phosphoric acid ($H_3PO_4$), sulfuric acid

($H_2SO_4$), nitric acid ($HNO_3$), sodium carbonate ($Na_2CO_3$), sodium orthophosphate ($Na_3HPO_4$) and 1H,1H,2H,2H-Perfluorodecyltrichlorosilane (FDTS) ($C_{10}H_4Cl_3F_{17}Si$) were purchased from Sigma Aldrich and were used without further purification.

## Surface preparation

To remove any organic contaminants, the aluminium substrates (2 cm $\times$ 2 cm) were first degreased with acetone for 10 minutes, followed by rinsing in deionized (DI) water. Then, the surfaces were polished in two different steps to reduce the surface roughness, chemical and electrochemical polishing.

### *Chemical polishing*

First, the degreased aluminium substrates were polished by dipping them in a mixture of phosphoric and nitric acids (6:1 by volume) for 6 minutes at 80 °C with strong stirring. Next, the surfaces were thoroughly rinsed with DI water.

### *Electrochemical polishing*

To further reduce the surface roughness, the chemically polished surfaces were subjected to electrochemical polishing. This step was performed using an aqueous solution of $Na_2CO_3$ and $Na_3HPO_4$ as the electrolyte. The chemically polished aluminium substrates were connected to the positive terminal whereas a platinum gauze to the negative terminal of a DC power supply. The power supply was set to 16 V resulting in the current density of 0.125 A/cm$^2$. The polishing was performed for ~15 minutes while maintaining the electrolyte at ~80 °C and agitating it vigorously through mechanical stirring using a magnetic stirrer plate. After completing the process, the surfaces were first neutralized in mild acidic solution and then extensively rinsed in DI water.

***Anodization***

To achieve different morphologies, i.e. nanoporous textures, the anodization was carried out whether in oxalic or sulfuric acid-based electrolytes; these will be referred as 'oxalic' and 'sulfuric' surfaces in the ensuing discussion. In both cases, the aluminium substrates served as anodes and a platinum gauze was used as cathodes. In addition, both oxalic and sulfuric electrolytes were stirred continuously, had the same molar concentration of 0.3 M and in both cases, the anodization was performed for 1 hour. The anodization in the oxalic acid was done at 120 V at ~5 °C, whereas, the anodization in the sulfuric acid was conducted at 19 V and at room temperature (~22 °C). The reason for choosing different working parameters (voltages and temperatures) is that the control of the surface morphology is achieved via triggering the self-ordering phenomenon which can occur during the fabrication of $Al_2O_3$. However, as also reported in [21], the self-ordering regime can occur only when the anodization is carried out within a narrow parametrical window. In other words, different electrolytes require different working conditions.

## Pore widening

After the anodization, the nanoporous aluminium substrates were immersed in a 5 weight% phosphoric acid solution at room temperature. This resulted in the pore wall being gradually etched away. The etching durations had to be optimized since the thickness of the wall separating two adjacent pores and the overall thickness of the oxide layer change with respect to the electrolyte and the anodization conditions. In our case, the porous morphologies are achieved after 15 and 120 minutes of pore widening of the sulfuric ('fp') and oxalic ('cp') surfaces, respectively. To obtain the fibrous structures, the etching duration was continued for additional 15 and 60 minutes for sulfuric ('df) and oxalic ('sf') surfaces, respectively (see Figure 2).

## Surface functionalization

The last step in surface preparation was to apply a self-assembled monolayer of FDTS on the anodized surfaces. This was done by dipping the surfaces in a 1.43 M solution of FDTS in hexane for 2 hours. Afterwards, the coated surfaces were baked at 110 °C for ~1 hour. For comparisons, the 'untreated' and 'polished only' aluminium substrates were also functionalized in the same way.

## Contact angle measurements

An in-house goniometer setup was used to measure advancing and receding contact angles [22].

## Free-falling water droplet impact tests

Water droplets of ~2.5 mm size were generated using a nozzle connected to a syringe pump. The highest drop velocity achieved was ~3 m/s, with droplets released from 60 cm height. Beyond this height, the precision of the impact location on the substrate was insufficient (due to gentle air movement in the laboratory). This made it difficult to fit the spreading droplet onto the substrate coupons. Each droplet impact was recorded (side-view) with a high-speed camera (Phantom V411) at 10,000 fps and then visually inspected to see whether the drops had fully rebounded or not.

## Freezing delay experiments

All surfaces were subjected to a freezing delay test in a custom designed cooling chamber (Figure 1). The surfaces were placed on a rotary stage at room temperature. Then, the cover was shut and pressed with bolts so that the chamber was well insulated from the outside. During the experiment, the ambient and the stage temperatures were recorded. The temperature of the coupons was assumed to be the same as of the rotary stage since the thermal inertia of the stage is a few orders of magnitude greater than of the thin aluminium coupons ($\sim 0.5$ vs $\sim 120$ $[J/K]$). Next, the chamber was rapidly brought to ~0 °C (we made sure that the difference between the stage and the

ambient temperatures was less than 0.5 °C). Then, ~10 µl water droplets were gently positioned on the substrates, each surface accommodated 4 to 5 drops. Finally, the chamber temperature was slowly reduced from 1 °C to -25 °C at a temperature rate of ~ 0.3 °C/min, this ensured a gentle, quasi-steady reduction in the temperature reduction without introducing any appreciable thermal gradients between droplets and the surroundings [4]. During the experiment, the relative humidity inside the chamber was between 60% and 40%. Finally, the temperature of the stage was recorded when the droplets turned into ice, and presented in Figure 5.

Upon freezing there is clear change in grayscale intensity of the droplet being imaged; the freezing interface of the inside the droplets (especially in the thermally controlled freezing stage) is clearly visible in our images. We used this optical imaging technique to detect droplet freezing.

## Results and Discussion

In general, it is challenging to control the surface morphology on a nanoscale level throughout a scalable fabrication process. The electrochemical approach adopted in this work has characteristic advantages to this end. Figure 2 shows the morphology of various nanoengineered samples produced in this work.

The ability to tune the contact area between a droplet and a surface (by changing the solid fraction) is instrumental because it has a direct impact on the nucleation temperature of the freezing droplets. Following the electrochemical surface texturing (Figure 2), surface functionalisation was used to render the surfaces hydrophobic. To characterize the wettability of the surfaces, advancing and receding contact angles were measured and are presented in Figure 3. From the figure, we see that the only surface that facilitates droplet roll-off is ‘sf’ since it is the only one which showed receding contact angles. The rest of the surfaces, despite having high advancing contact angles, did not

present any receding contact angles, meaning that the droplets were pinned.

The morphology images in Figure 2 only offer a qualitative estimate of the variation in the surface solid fraction and do not capture the three-dimensional droplet/surface interface. Therefore, the advancing contact angles were used to estimate the solid fraction of the surfaces by employing equation (1), i.e. the Cassie equation

$$\cos\theta_A = -1 + \phi(1 + \cos\theta_A^*) \quad (1)$$

where $\theta_A^*$, $\theta_A$ and $\phi$ represent the advancing contact angle on a smooth functionalized aluminium surface, the measured contact angle and the solid fraction, respectively.

Next, to get the first impression of the drop impalement resistance of our surfaces, we conducted drop impact tests at room temperature. The results of these free-falling water drop impact experiments are presented in Figure 4. Drops were released from different heights between 15 cm and 60 cm, at 15 cm intervals. To ensure reproducibility, the surfaces were manufactured in different batches. All surfaces but 'sf', showed impalement at a velocity of ~1.5 m/s (corresponding Weber number, $We$~ 80). 'sf' surfaces did not show impalement up to the velocity of ~3 m/s ($We$~ 300).

It can be readily seen how impact results (pinning or rebound) are affected by increasing the receding contact angle and solid fraction from equations (2) and (3) [23, 24]

$$F_C \sim 2\pi\gamma_{LG}R(t)[1 - cos\theta_R] \quad (2)$$

where $F_C, \gamma_{LG}, R(t)$ and $\theta_R$ are the capillary force which is responsible for pulling the lamella back, the liquid-gas surface energy, the changing radius of the liquid disk after the impact and the

receding contact angle, respectively.

$$\dot{E}_{diss} \propto \mu \frac{\partial V}{\partial y} AV \tag{3}$$

where $\mu, A$ and $V$ are the liquid viscosity, the liquid-solid contact area and the velocity of the moving lamella. The drop impact scenarios can be broken down into spreading (to form a lamella) and receding of the droplet volume on the substrate [25], along with penetration of the part of the drop meniscus into the surface texture near the point of impact. The meniscus penetration can be partial or complete as will be discussed below. During the spreading stage, the kinetic energy is either stored as surface energy or dissipated through viscous forces which are shear (between the spreading lamella and the surface) and drag (between the lamella and air). During the retraction stage, the surface energy is partially converted back into kinetic energy and the remnant is again dissipated through viscous forces. If the overall dissipated energy is not too large and the contact-line is not pinned, the regained kinetic energy can lead to a full rebound [26, 27]. This essentially suggests that the transition from pinning ('df', 'cp' and 'fp') to a complete rebound scenario ('sf') in Figure 4 was in fact induced by increasing the surface non-wetting (i.e. high contact angle as well as low hysteresis, c.f. Figure 3).

The impalement of the droplet meniscus into the surface texture (near the point of impact) can be partial or complete, depending on the impact velocity. Starting with a low value, as the impact velocity is progressively increased, the partial penetrating meniscus is able to push out the air locked in the asperities and keep penetrating further. When the impact velocity reaches a critical value ($V_C$), the meniscus touches the bottom of the asperities and sticks [28]. Therefore, at some point, all surfaces will be penetrated, and in the case of 'sf' it happened around $V_C = 3m/s$.

From Figure 5, we see that the highest median nucleation temperature was recorded on the 'un' surfaces, lower nucleation temperatures were observed on the superhydrophobic surfaces ('sf', 'df', 'cp' and 'fp') and the lowest was observed on the 's' surfaces. There are two points which should be addressed: why the results are not more distinctive, and what explains the observed trend?

It is reasonable to expect that nucleation temperatures should be related to a water-surface contact area. In other words, as will be discussed below, superhydrophobic surfaces with higher contact angles should exhibit lower nucleation temperatures. However, from the nucleation theory, ice nucleation depends not only on the surface wettability, i.e. surface energy but also quite dramatically on the roughness radius of curvature $R_a$ [4]. In fact, the critical nucleation radius of an ice germ is a function of ice-water interfacial energy and the volumetric free energy. Once the radius of an ice germ exceeds the critical radius, a stable ice embryo is formed turning metastable (supercooled) water into ice. Therefore, in order to influence the nucleation temperature, $R_a$ has to be reduced to the same order of magnitude as the critical ice nucleus ($r_c$), which is around 2 nm at – 20 $°C$ [29].

The average freezing delay time ($\tau_{avg}$) required for ice nucleation (at a constant temperature $T_S$) can be expressed as [29]

$$\tau_{avg} \propto \frac{1}{J_\Phi} \tag{4}$$

where $J_\Phi$ is the nucleation rate. From equation (4) we can readily see that when the nucleation

rate is reduced, the inception of nucleation is delayed. Equation (5) shows how $J_\Phi$ is influenced by the wettability of surfaces. The derivation of the expression for $J_\Phi$ can be found elsewhere [4, 30, 31]

$$J_\Phi = \Phi \cdot \frac{k_B\ T_S\ n}{h} \cdot exp\left( -\frac{E_R\quad T_S}{(T_S - T_R)^2} - \frac{1}{k_B\ T_S} \cdot \frac{16\pi\ \gamma_{IW}^3\ {T_m}^2}{3(\ T_m - \ T_S)^2 \Delta {H_v}^2} \cdot f(\theta_A\ , R_a) \right) \quad (5)$$

where $\Phi, k_B, T_S,\ T_m, n, h, \gamma_{IW}, \Delta H_v, f$ and $R_a$ are the droplet-substrate contact area fraction, the Boltzmann constant, the temperature of the substrate (and of the droplet), the equilibrium melting temperature of ice at 1 atm, the density of water molecules at the ice-water interface, the Planck constant, the ice-water interfacial energy, the volumetric enthalpy of fusion for water, the wetting coefficient and the roughness curvature radius, respectively. $E_R$ and $T_R$ are experimentally determined constants.

From equation (5) we see that the nucleation rate depends exponentially on $f(\theta_A\ , R_a)$ and linearly on $\Phi$ (which is in our case, assuming the droplet remains in the Cassie state, equals to $\phi$). To minimize $J_\Phi$, we should maximize $f$, and its maximum value ($f = 1$) corresponds to homogeneous nucleation. Figure 6 shows how $f$ varies with respect to $\theta_A$ and $R_a$, see [29] for further details and exact analytical expression.

From Figure 6, we see the wetting factor is strongly affected both by the contact angle and by the surface roughness. In the case of the superhydrophobic vs untreated ('un') surfaces, higher $\theta_A$ angles of the former result in higher wetting coefficients. In addition, the solid fraction of the superhydrophobic surfaces is at least four times lower than that of 'un' surfaces ($\phi_{un} \approx 0.97$). Altogether, these lead to lower $J_\Phi$ values on the superhydrophobic surfaces (see Figure 7). In case

of smooth ('s') surfaces, the mean root square roughness was measured between 5 and 20 nm, meaning that $R_a/r_c < 10$ which considerably increases the wetting coefficient.

Furthermore, as can be seen in Figure 7, nucleation is strongly affected by the temperature at which the process takes place. So, if the process temperature is reduced by roughly 2 °C, the nucleation rate will be increased by 2 orders of magnitude. In other words, even if the surfaces have different nucleation temperatures, observing it through an experiment where the temperature keeps changing will be hard.

Thus, freezing delay measurements conducted at a constant temperature may lead to more distinctive results showing which surfaces can longer delay nucleation. Finally, the difference between surface morphologies and the advantage of the superhydrophobic surfaces should become evident when features such as ice adhesion strength and drop impact in cold environments are considered. These aspects are currently under investigation, to be reported elsewhere in the future.

# Conclusions

In this work, we followed a scalable process to prepare aluminium based nanotextured surfaces for anti-icing application. Nucleation temperature measurements were used to evaluate the icephobicity of the surfaces. Additionally, drop impact tests at room temperature were used to assess the impalement resistance and dynamic stability of the surfaces. Overall, our results provide a rational approach to engineer aluminium based icephobic surfaces and provide preliminary assessments of the icephobic behaviour. Future works will concentrate on ice adhesion and impact tests in supercooled conditions.

# Acknowledgements

The work was partially supported by M.K.T.'s EPSRC First Grant (EP/N006577/1) and from the European Research Council (ERC) under the European Uninon's Horizon 2020 research and innovation programme under grant agreement no. 714712.


# Nomenclature

| | |
|---|---|
| $A$ | area, $m^2$ |
| AFM | atomic force microscope |
| CA | contact angle, $^\circ$ |
| CAH | contact angle hysteresis, $^\circ$ |
| 'cp' | coarse-pores |
| DI | deionized water |
| 'df' | dense-fibres |
| $\dot{E}_{diss}$ | dissipated energy, $Watt$ |
| $E_R$ | experimentally determined constant, $K$ |
| $F_C$ | capillary force, $N$ |
| FDTS | 1H,1H,2H,2H-Perfluorodecyltrichlorosilane |
| $f_c$ | wetting factor of a spherically convex surface, $dimensionless$ |
| 'fp' | fine-pores |
| $h$ | Planck's constant, $kg \cdot m^2/s$ |
| $J_\Phi$ | nucleation rate, $molecules/s \cdot m^2$ |
| $k_B$ | Boltzmann constant, $kg \cdot m^2/s^2 \cdot K$ |

| | |
|---|---|
| $n$ | density of water molecules at the ice-water interface, $molecules/m^2$ |
| $R$ | radius of the liquid disk, $m$ |
| $R_a$ | roughness radius of curvature, $m$ |
| $r_c$ | critical ice nucleus, $m$ |
| 's' | smooth |
| 'sf' | sparse-fibres |
| $T_m$ | melting temperature of ice at 1 atm, $K$ |
| $T_N$ | median nucleation temperature, $K$ |
| $T_R$ | experimentally determined constant, $K$ |
| $T_S$ | temperature of the substrate, $K$ |
| t | time, $s$ |
| 'un' | untreated (not polished) |
| $V$ | velocity, $m/s$ |
| $V_C$ | critical velocity, $m/s$ |
| $We$ | Weber number, $dimensionless$ |
| x | ratio between $R_a$ and $r_c$, $dimensionless$ |
| y | length, $m$ |

Greek Symbols

| | |
|---|---|
| $\gamma_{IW}$ | ice-water surface energy, $J/m^2$ |
| $\gamma_{LG}$ | liquid-gas surface energy, $J/m^2$ |
| $\Delta H_v$ | water volumetric enthalpy of fusion, $J/m^3$ |

| | |
|---|---|
| $\theta_A$ | advancing contact angle, $^\circ$ |
| $\theta_A^*$ | advancing contact angle on a smooth surface, $^\circ$ |
| $\theta_R$ | receding contact angle, $^\circ$ |
| $\mu$ | dynamic viscosity of a liquid, $kg/m \cdot s$ |
| $\tau_{avg}$ | average time, $s$ |
| $\phi$ | solid fraction, $dimensionless$ |
| $\Phi$ | droplet-substrate contact area fraction, $dimensionless$ |

Molecular formulas

| | |
|---|---|
| $Al_2O_3$ | aluminium oxide |
| $C_2H_2O_4$ | oxalic acid |
| $C_{10}H_4Cl_3F_{17}Si$ | 1H,1H,2H,2H-Perfluorodecyltrichlorosilane |
| $HNO_3$ | nitric acid |
| $H_3PO_4$ | phosphoric acid |
| $H_2SO_4$ | sulfuric acid |
| $Na_2CO_3$ | sodium carbonate |
| $Na_3HPO_4$ | sodium orthophosphate |

# References


[1] M. A. Rahman and A. M. Jacobi, “Condensation, Frost Formation, and Frost Melt-Water Retention Characteristics on Microgrooved Brass Surfaces Under Natural Convection,” *Heat Transf. Eng.*, vol. 34, no. 14, pp. 1147–1155, 2013.

[2] S. Yoon, G. Hayase, and K. Cho, “Measurements of Frost Thickness and Frost Mass on a Flat Plate under Heat Pump Condition,” *Heat Transf. Eng.*, vol. 31, no. 12, pp. 965–972, 2010.

[3] NZ CAA, *Aircraft Icing Handbook*, 1st ed. Civil Aviation Authority, New Zealand, 2000.

[4] P. Eberle, M. K. Tiwari, T. Maitra, and D. Poulikakos, “Rational nanostructuring of surfaces for extraordinary icephobicity,” *Nanoscale*, vol. 6, no. 9, pp. 4874–81, 2014.

[5] K. Golovin *et al.*, “Designing durable icephobic surfaces,” *Sci. Adv.*, vol. 2, no. 3, pp. 1–12, 2016.

[6] H. Sojoudi, M. Wang, N. D. Boscher, G. H. McKinley, and K. K. Gleason, “Durable and scalable icephobic surfaces: similarities and distinctions from superhydrophobic surfaces,” *Soft Matter*, vol. 12, no. 7, pp. 1938–1963, 2016.

[7] T. M. Schutzius *et al.*, “Physics of icing and rational design of surfaces with extraordinary icephobicity,” *Langmuir*, vol. 31, no. 17, pp. 4807–4821, 2015.

[8] E. Mitridis *et al.*, “Metasurfaces leveraging solar energy for icephobicity,” *ACS Nano*, vol. 12, no. 7, pp. 7009–7017, 2018.

[9] S. Dash, J. de Ruiter, and K. K. Varanasi, “Photothermal trap utilizing solar illumination for ice mitigation,” *Sci. Adv.*, vol. 4, no. 8, pp. 1–7, 2018.

[10] M. J. Kreder, J. Alvarenga, P. Kim, and J. Aizenberg, “Design of anti-icing surfaces: Smooth, textured or slippery?,” *Nat. Rev. Mater.*, vol. 1, no. 1, pp. 1–15, 2016.

[11] L. Mishchenko *et al.*, “Design of ice-free nanostructured surfaces based on repulsion of

impacting water droplets," *ACS Nano*, vol. 4, no. 12, pp. 7699–7707, 2010.

[12] H. Saito, K. Takai, and G. Yamauchi, "Water and ice repellent coatings," *Surf. Coatings Int.*, vol. 80, no. 4, pp. 168–171, 1997.

[13] S. A. Kulinich and M. Farzaneh, "Ice adhesion on super-hydrophobic surfaces," *Appl. Surf. Sci.*, vol. 255, no. 18, pp. 8153–8157, 2009.

[14] S. Bengaluru Subramanyam, V. Kondrashov, J. Rühe, and K. K. Varanasi, "Low ice adhesion on nano-textured superhydrophobic surfaces under supersaturated Conditions," *ACS Appl. Mater. Interfaces*, vol. 8, no. 20, pp. 12583–12587, 2016.

[15] P. Tourkine, M. Le Merrer, and D. Quéré, "Delayed freezing on water repellent materials," *Langmuir*, vol. 25, no. 13, pp. 7214–7216, 2009.

[16] Y. Wang, J. Xue, Q. Wang, Q. Chen, and J. Ding, "Verification of icephobic/anti-icing properties of a superhydrophobic surface," *ACS Appl. Mater. Interfaces*, vol. 5, no. 8, pp. 3370–3381, 2013.

[17] L. Cao, A. K. Jones, V. K. Sikka, J. Wu, and D. Gao, "Anti-icing superhydrophobic coatings," *Langmuir*, vol. 25, no. 21, pp. 12444–12448, 2009.

[18] A. Alizadeh *et al.*, "Dynamics of ice nucleation on water repellent surfaces," *Langmuir*, vol. 28, no. 6, pp. 3180–3186, 2012.

[19] S. Jung, M. K. Tiwari, and D. Poulikakos, "Frost halos from supercooled water droplets.," *Proc. Natl. Acad. Sci. U. S. A.*, vol. 109, no. 40, pp. 16073–8, 2012.

[20] T. Kikuchi *et al.*, "Ultra-high density single nanometer-scale anodic alumina nanofibers fabricated by pyrophosphoric acid anodizing," *Sci. Rep.*, vol. 4, pp. 1–6, Dec. 2014.

[21] W. Lee, R. Ji, U. Gösele, and K. Nielsch, "Fast fabrication of long-range ordered porous alumina membranes by hard anodization," *Nat. Mater.*, vol. 5, pp. 741–747, Sep. 2006.

[22] C. Peng, Z. Chen, and M. K. Tiwari, “All-organic superhydrophobic coatings with mechanochemical robustness and liquid impalement resistance,” *Nat. Mater.*, vol. 17, no. 4, pp. 355–360, 2018.

[23] T. Maitra *et al.*, “Supercooled water drops impacting superhydrophobic textures,” *Langmuir*, vol. 30, no. 36, pp. 10855–10861, 2014.

[24] D. Bartolo, C. Josserand, and D. Bonn, “Retraction dynamics of aqueous drops upon impact on non-wetting surfaces,” *J. Fluid Mech.*, vol. 545, pp. 329–338, Sep. 2005.

[25] A. L. Yarin, “Drop impact dynamics: splashing, spreading, receding, bouncing…,” *Annu. Rev. Fluid Mech.*, vol. 38, no. 1, pp. 159–192, 2006.

[26] C. Clanet, C. Béguin, D. Richard, and D. Quéré, “Maximal deformation of an impacting drop,” *J. Fluid Mech.*, vol. 517, pp. 199–208, Jun. 2004.

[27] I. V. Roisman, R. Rioboo, and C. Tropea, “Normal impact of a liquid drop on a dry surface: Model for spreading and receding,” *Proc. R. Soc. A Math. Phys. Eng. Sci.*, vol. 458, no. 2022, pp. 1411–1430, 2002.

[28] T. Maitra *et al.*, “On the nanoengineering of superhydrophobic and impalement resistant surface textures below the freezing temperature,” *Nano Lett.*, vol. 14, no. 1, pp. 172–182, 2014.

[29] H. R. Pruppacher, J. D. Klett, and P. K. Wang, *Microphysics of Clouds and Precipitation*. D. Reidel Publishing Company, Dordrecht, Holland, 1978.

[30] R. Zhang, P. Hao, X. Zhang, and F. He, “Supercooled water droplet impact on superhydrophobic surfaces with various roughness and temperature,” *Int. J. Heat Mass Transf.*, vol. 122, pp. 395–402, Feb. 2018.

[31] S. Jung *et al.*, “Are superhydrophobic surfaces best for icephobicity?,” *Langmuir*, vol. 27, no. 6, pp. 3059–3066, 2011.

# List of Figure Captions

Figure 1: (A) Top and (B) cross-section views of the cooling chamber. The cooling chamber components are a heat exchanger through which a liquid coolant flows (1), fans to improve the convection (2), a rotary platform to accommodate multiple surfaces (3), a Peltier module to enable independent temperature control of the stage (4). In addition, 3 humidity sensors were placed over the stage (circles). Finally, the stage and ambient temperatures are measured. Multiple thermocouples were placed close to the stage to ensure that the air temperature at the coupons was measured accurately (asterisks).

Figure 2: Atomic force microscope (AFM) images (top row) of four different morphologies, featuring sparse-fibres ('sf'), dense-fibres ('df'), coarse-pores ('cp') and fine-pores ('fp'), respectively. The bottom row of images shows characteristic line profiles from the AFM images in the top row to highlight the width and the height of the nanostructures.

Figure 3: Advancing ($\theta_A$) and receding ($\theta_R$) water contact angles measured on 'sf', 'df', 'cp' and 'fp' surfaces. The missing receding angle bars for a number of morphologies indicated the cases where the droplet was pinned to the substrates and the contact line did not recede.

Figure 4: Results of water droplet impact test on different surfaces. All surfaces but 'sf' showed penetration at the experimental minimum impact velocities of 1.5 m/s, which means low impalement threshold and are marked by downward arrows. 'sf' surface didn't show impalement even at the maximum drop velocity of 3 m/s (indicated by an upward arrow).

Figure 5: Box plot of nucleation temperatures measured on different surfaces. The abbreviations 's' and 'un' denote the smooth (polished only) and untreated surfaces, respectively. The box size represents the first and third quartile of the measured temperatures, the line inside the box describes the median nucleation temperature ($T_N$) and the whiskers denote the outliers. The $T_N$ is

substantially below 0 °C on all surfaces, and the difference between treated and untreated surfaces being several degrees. This is known to make orders of magnitude difference in terms of time taken for droplets to freeze at a given temperature, as reported by Eberle et al. [4].

Figure 6: Wetting factor of a spherically convex surface ($f_C$) is plotted against the ratio $R_a/r_c$ for varying $\theta_A$ values.

Figure 7: Ice nucleation rate ($J_\Phi$) as a function of substrate temperature ( $T_S$) for (A) different $\theta_A$ and (B) $R_a$ values.

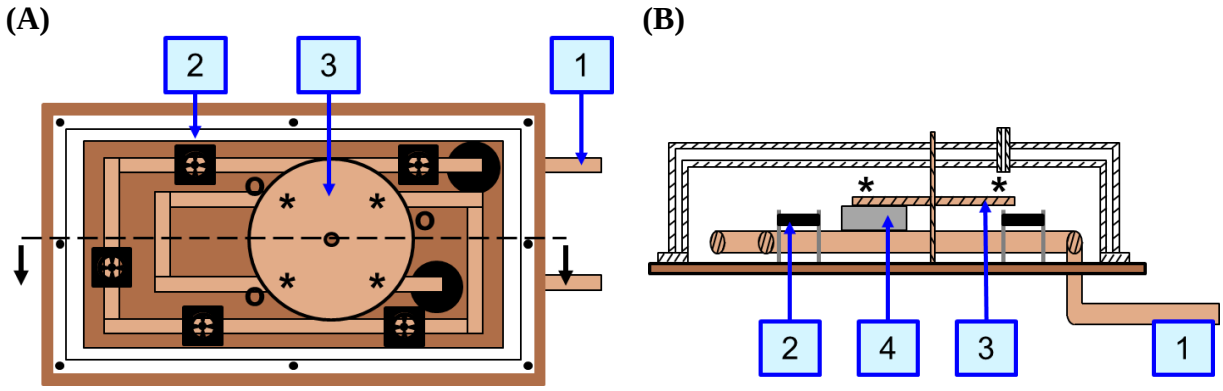


**Figure 1**: (A) Top and (B) cross-section views of the cooling chamber. The cooling chamber components are a heat exchanger through which a liquid coolant flows (1), fans to improve the convection (2), a rotary platform to accommodate multiple surfaces (3), a Peltier module to enable independent temperature control of the stage (4). In addition, 3 humidity sensors were placed over the stage (circles). Finally, the stage and ambient temperatures are measured. Multiple thermocouples were placed close to the stage to ensure that the air temperature at the coupons was measured accurately (asterisks).

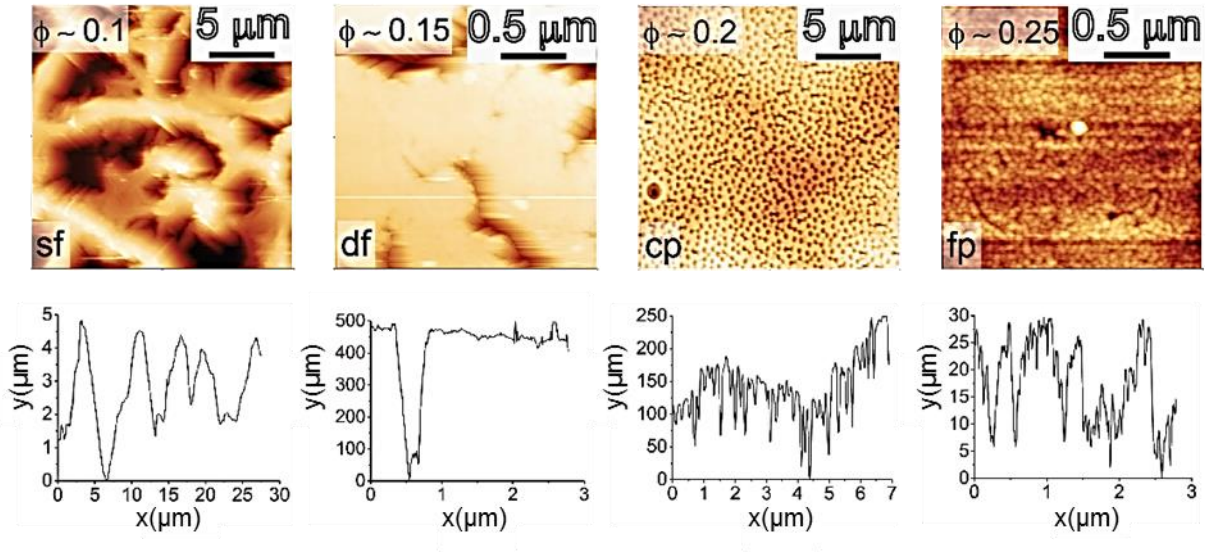


**Figure 2**: Atomic force microscope (AFM) images (top row) of four different morphologies, featuring sparse-fibres ('sf'), dense-fibres ('df'), coarse-pores ('cp') and fine-pores ('fp'), respectively. The bottom row of images shows characteristic line profiles from the AFM images in the top row to highlight the width and the height of the nanostructures.

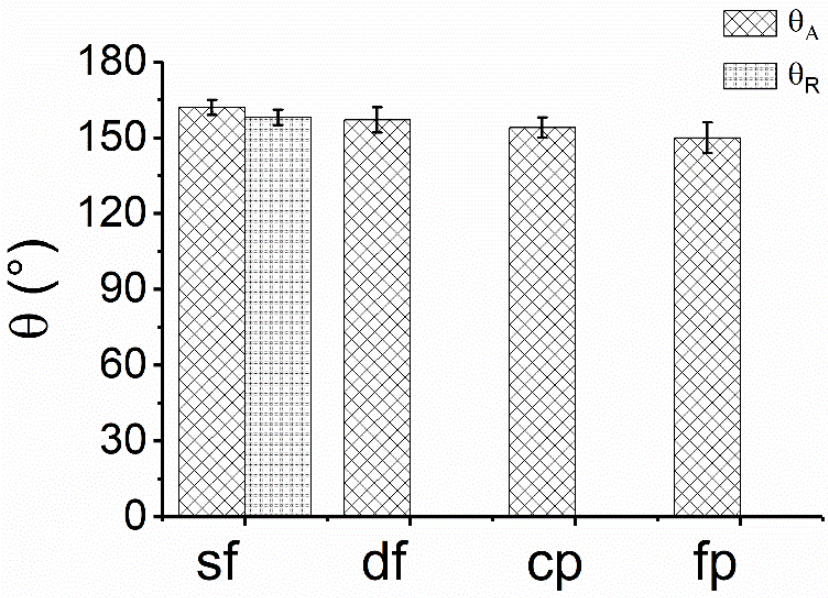


**Figure 3:** Advancing ($\theta_A$) and receding ($\theta_R$) water contact angles measured on 'sf', 'df', 'cp' and 'fp' surfaces. The missing receding angle bars for a number of morphologies indicated the cases where the droplet was pinned to the substrates and the contact line did not recede.

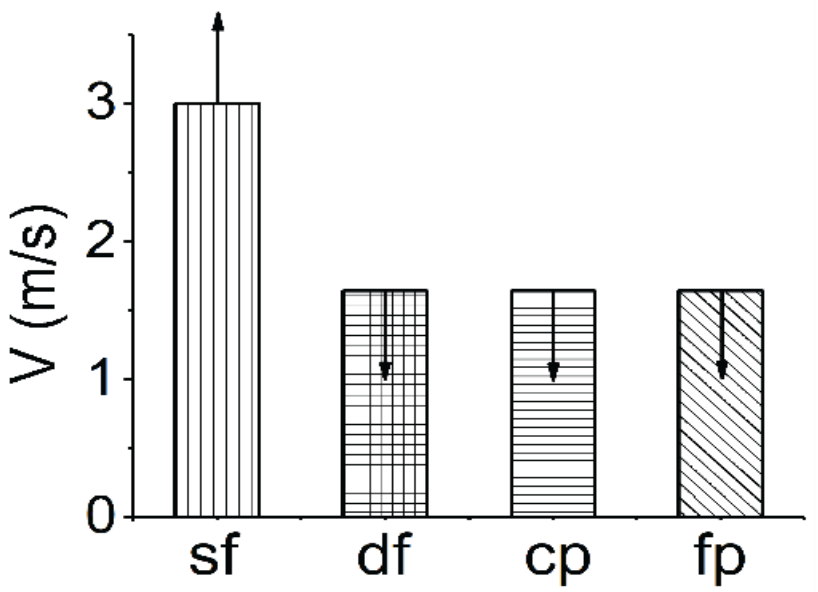


**Figure 4**: Results of water droplet impact test on different surfaces. All surfaces but 'sf' showed penetration at the experimental minimum impact velocities of 1.5 m/s, which means low impalement threshold and are marked by downward arrows. 'sf' surface didn't show impalement even at the maximum drop velocity of 3 m/s (indicated by an upward arrow).

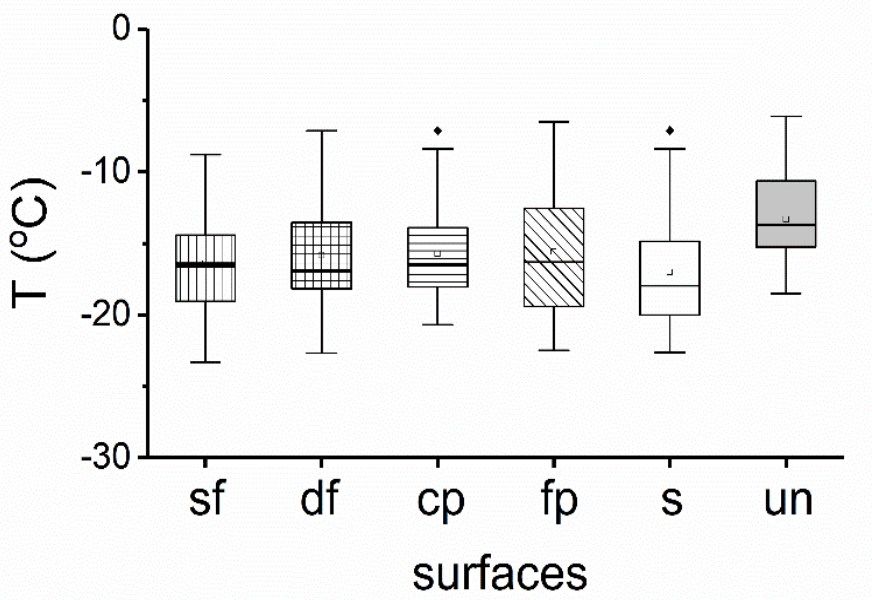


**Figure 5**: Box plot of nucleation temperatures measured on different surfaces. The abbreviations 's' and 'un' denote the smooth (polished only) and untreated surfaces, respectively. The box size represents the first and third quartile of the measured temperatures, the line inside the box describes the median nucleation temperature ($T_N$) and the whiskers denote the outliers. The $T_N$ is substantially below 0 °C on all surfaces, and the difference between treated and untreated surfaces being several degrees. This is known to make orders of magnitude difference in terms of time taken for droplets to freeze at a given temperature, as reported by Eberle et al. [4].

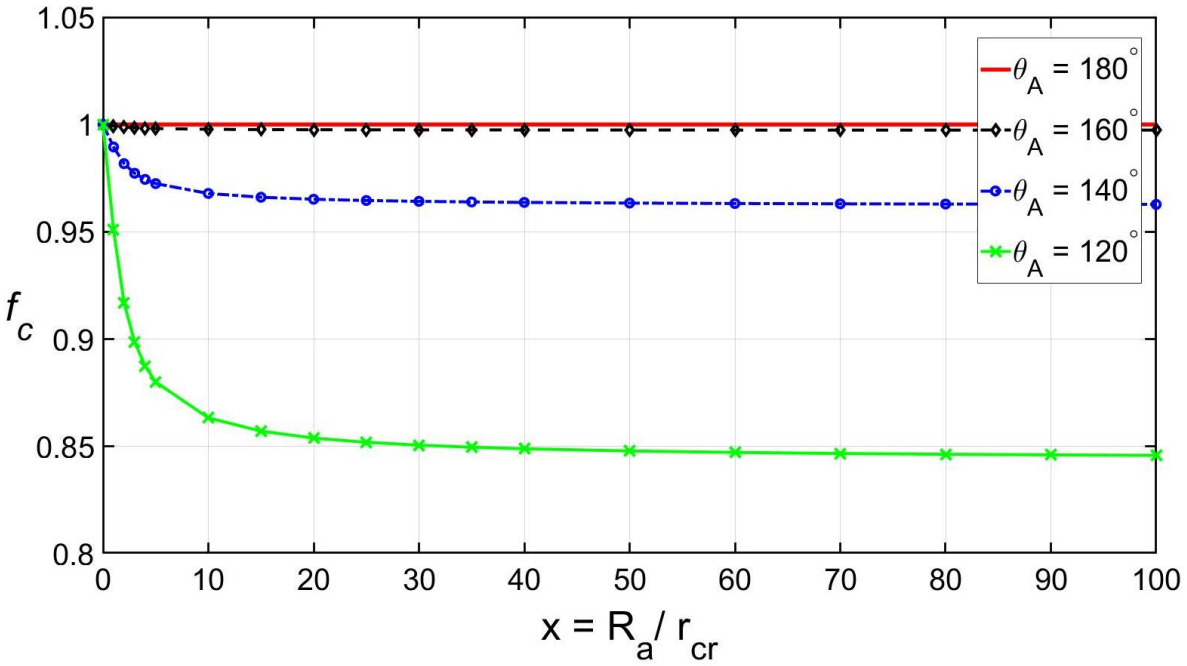


**Figure 6**: Wetting factor of a spherically convex surface ($f_C$) is plotted against the ratio $R_a/r_c$ for varying $\theta_A$ values.

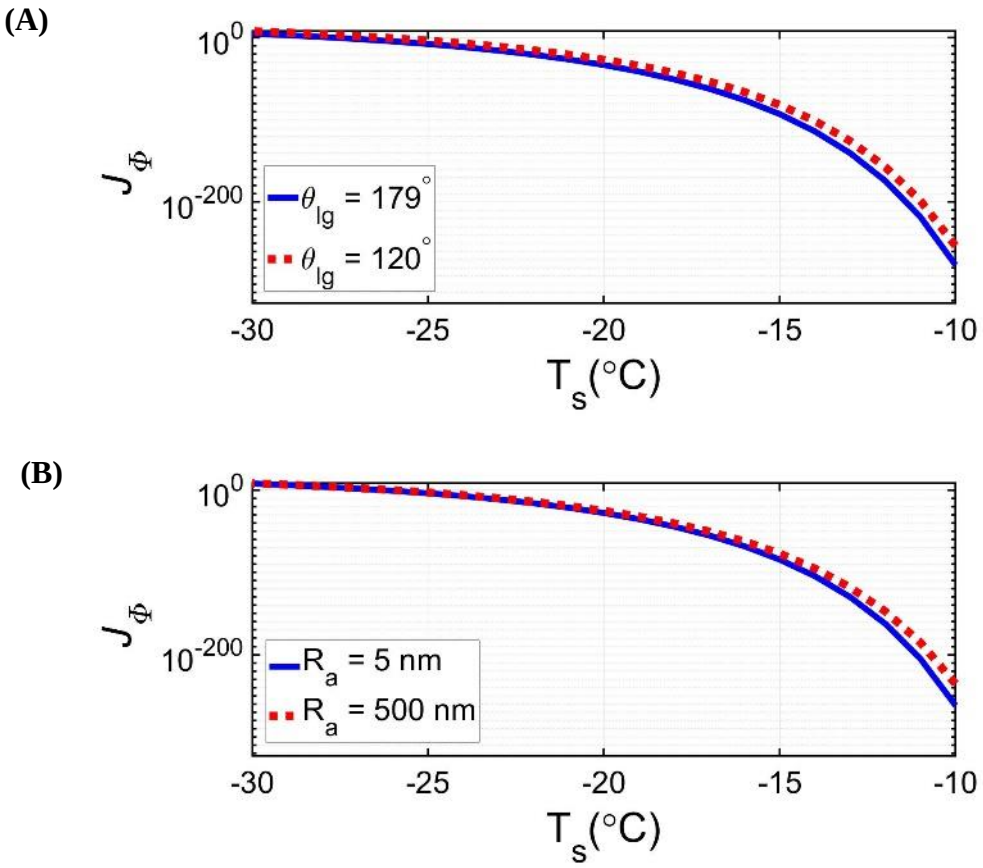


**Figure 7**: Ice nucleation rate ($J_\Phi$) as a function of substrate temperature ( $T_S$) for (A) different $\theta_A$ and (B) $R_a$ values.

# Biography

Michael Grizen is investigating interfacial phenomena and phase change processes. Beforehand, Michael worked for four years as a thermal engineer in the space industry. He received his Bachelor (summa cum laude) and M.Sc. (direct track) from Tel-Aviv University. During his M.Sc. studies, he carried out research in the field of solar radiation harvesting. His PhD project involves experimental investigation of ice nucleation and impact of cold droplets on nanoengineered surfaces. Through a better understanding of the nucleation process combined with rationally manufactured surfaces, he hopes to efficiently suppress ice and frost formation.

Tanmoy Maitra is a Materials Scientist (Specialist) at FT Technologies UK. His current work focuses on the evaluation and implement materials and solutions to improve the performance of high-performance acoustic resonance wind sensors. He obtained his PhD from ETH Zurich, Switzerland. After graduating, he joined as a Postdoctoral Fellow at Stanford University with a Swiss National Science Foundation (SNSF) Fellowship. After that, he moved to University College London (UCL) as a Research Associate to work on multifunctional superhydrophobic materials, icephobicity and additive manufacturing. He has published papers in high-quality journals and presented in several international conferences in the area of thermal-fluid sciences. He represented UCL to the prestigious Global Young Scientist Summit (GYSS) in Singapore in 2018. He was also awarded ETH medal (2016) for his doctoral thesis, Ambuja's Young Researcher Award (2012) for one of the best master's thesis in India, and Academic Excellence Award (2009-2010) in Indian Institute of Technology, Kanpur.

Jeremy P. Bradley studied Materials Science and Technology at Brunel University graduating in 1997. He then worked for the Defense Evaluation Research Agency (DERA) in Farnborough as a research scientist. After a short period as a Technical Salesperson for Olympus Optical UK, he joined Airbus as a materials specialist. Currently he is the Head of Corrosion prevention principles and sealing for all aircraft. During his time at Airbus he has been heavily involved in materials research including new sealant chemistries, novel sealing methods and functional coatings for aerodynamic performance, anti-ice and self-cleaning properties.

Manish K Tiwari is a Professor of Nanoengineering in the Mechanical Engineering Department of

the University College London and directs the Nanoengineered Systems Laboratory. His group focuses on the physics of small-scale transport phenomena and nanomanufacturing technologies, to underpin new developments in energy and healthcare applications. He has published papers in high-quality journals such as Nature Materials, Nature Communications, PNAS, Nano Letters etc. He is an European Research Council (ERC) Starting Grant Awardee and a member of the EPSRC Early Career Forum in Manufacturing Research.